Journal of Catalysis 269 (2010) 281–290

Contents lists available at ScienceDirect

Journal of Catalysis

journal homepage: www.elsevier.com/locate/jcat

Efficient and stable oxidative steam reforming of ethanol for hydrogen production: Effect of *in situ* dispersion of Ir over Ir/La_2O_3

Hongqing Chen [a], Hao Yu [a,*], Feng Peng [a,*], Hongjuan Wang [a], Jian Yang [a], Minqiang Pan [b]

[a] School of Chemistry and Chemical Engineering, South China University of Technology, Guangzhou 510640, People's Republic of China
[b] School of Mechanical Engineering, South China University of Technology, Guangzhou 510640, People's Republic of China

ARTICLE INFO

Article history:
Received 7 July 2009
Revised 6 November 2009
Accepted 8 November 2009
Available online 30 December 2009

Keywords:
Hydrogen production
Oxidative steam reforming
Ethanol
Ir/La_2O_3
In situ dispersion
Coking
Sintering

ABSTRACT

La_2O_3-supported Ir catalyst was prepared by wetness impregnation method for the oxidative steam reforming of ethanol (OSRE). Fresh, reduced, and used catalysts were characterized by N_2 adsorption, H_2 chemisorption, XRD, FT-IR, TEM, and XPS. La_2O_3 would transform into hexagonal $La_2O_2CO_3$ during OSRE, which suppress coking effectively. Reduced Ir metal can interplay with $La_2O_2CO_3$ to form Ir-doped $La_2O_2CO_3$. It dynamically forms and decomposes to release active Ir nanoparticles, thereby preventing the catalyst from sintering and affording high dispersion of Ir/La_2O_3 catalysts at elevated temperatures. By introducing ultrasonic-assisted impregnation method during the preparation of a catalyst, the surface Ir concentration was significantly improved, while the *in situ* dispersion effect inhibited Ir from sintering. The Ir/La_2O_3 catalyst prepared by the ultrasonic-assisted impregnation method is highly active and stable for the OSRE reaction, in which the Ir crystallite size was maintained at 3.2 nm after 100 h on stream at 650 °C and metal loading was high up to 9 wt%.

1. Introduction

Producing hydrogen with high efficiency and less environmental impact is highly desired for the growing fuel cell technique and industry [1–3]. Due to low toxicity and renewability, bio-ethanol is of great interest as a feedstock for hydrogen production. Hydrogen can be produced via steam reforming of ethanol (SRE) at 400–700 °C over supported metal catalysts [2,4]. However, this process frequently suffers from severe deactivation caused by coking and sintering. High $H_2O/EtOH$ ratio can decrease the coke deposition rate at the expense of energy efficiency [5]. Recently, Pereira et al. [6] reported that coke can also be removed through a repeated burning process. However, complicated control is necessary for the switchable reaction–regeneration operation. Operating at higher temperature or introducing modest oxygen in the reaction stream (Oxidation Steam Reforming, OSR) is helpful to depress the coke formation, while the thermal sintering of both active components and supports makes the issue more challenging [7–9].

Addition of alkaline [10], alkaline earth [11], and rare earth [12] oxides to catalysts can inhibit coking due to the cracking of ethylene. Due to the outstanding oxygen storage ability of CeO_2, the $Rh–CeO_2/Al_2O_3$ [13–15], $Ni–Rh/CeO_2$ [16], and Ir/CeO_2 [17] catalysts showed excellent activity and stability in reforming ethanol. It was proposed that the strong metal–CeO_2 interaction played an important role. It has been reported that the unique interaction between La_2O_3 and metal catalysts can depress the formation of coke [18]. Recently, Araujo et al. [19] proposed the possibility of La_2O_3 to enhance the dispersion of noble metal. Since the specific-surface-areas of these oxides are relatively low, they are frequently used to modify high specific-surface-area Al_2O_3 supports [12,20].

Compared with common Al_2O_3, the low-surface-area supports have preferable thermal stability. However, it is relatively difficult to introduce and stabilize active metals onto them with high dispersion. Under proper conditions, new complex species may be formed through the strong interaction between active metals and supports (SIMS) [19,21–23]. By the decomposition of these complexes, active metals can be *in situ* formed and delivered to improve the dispersion. For example, by reducing the perovskite-type $La_2NiO_4/LaNiO_3$, a well-dispersed Ni-supported La_2O_3 oxide can be obtained [24,25]. However, if the process is irreversible, the long-term stability cannot be achieved due to successive sintering.

La_2O_3 as a support has been widely investigated due to its thermal stability and diverse crystalline phases. Depending on catalyst preparation and active metals employed, lanthanum oxide species can transform into La_2O_3 [26], $La(OH)_3$ [27], tetragonal (I), monoclinic (Ia), and hexagonal (II) $La_2O_2CO_3$ [28,29]. Some of these phase transitions are reversible, such as $La_2O_3 + CO_2 \leftrightarrow La_2O_2CO_3$ at ~600 °C [30]. Verykios and co-workers have proved that the coke deposited on the interface between Ni and $La_2O_2CO_3$ may be gasified by: $La_2O_2CO_3 + C \rightarrow La_2O_3 + 2CO$ [18,31]. This reaction

* Corresponding authors. Fax: +86 20 8711 4916.
E-mail addresses: yuhao@scut.edu.cn (H. Yu), cefpeng@scut.edu.cn (F. Peng).

0021-9517/$ - see front matter © 2009 Elsevier Inc. All rights reserved.
doi:10.1016/j.jcat.2009.11.010

effectively suppresses coking of Ni/La_2O_3 catalyst in SRE. The SIMS effect between lanthanum species and active metals has also been observed by several authors [31–33]. Recently, it has been reported that Ni nanocrystallites were stabilized over $La_2O_2CO_3$, while they were aggregated over $La(OH)_3$ [27]. However, these unique interactions have not been fully elucidated yet. Thus, the in-depth understanding and delicate design for SIMS are essential and highly desired.

In this work, La_2O_3-supported Ir catalysts were employed to catalyze the OSRE reaction for hydrogen production. The resistance to coking and sintering of Ir/La_2O_3 at elevated temperatures was observed. We proposed that the excellent performance of Ir/La_2O_3 was due to the formation of $La_2O_2CO_3$ and an *in situ* dispersion effect of Ir on $La_2O_2CO_3$. Based on the insight to the SIMS between Ir and $La_2O_2CO_3$, a supersonic-assisted impregnation method was proposed. Due to the *in situ* dispersion effect, the resulting catalyst possessed enhanced OSRE performance in terms of the activity and stability.

2. Experimental section

2.1. Catalyst preparation

The Ir catalysts were prepared by impregnating appropriate amounts of iridium precursor ($IrCl_3{\cdot}nH_2O$, Ir content: 54.51 wt%, Shanghai July Chemical Co., Ltd., China) onto La_2O_3 (Sinopharm Chemical Reagent Co., Ltd.). The impregnated catalysts were dried at 120 °C overnight, and then calcined at 500 °C in air for 2 h. The loading of Ir was 9 or 4.8 wt% of catalyst. The resulting catalysts were denoted as $Ir(9)/La_2O_3$-i and $Ir(4.8)/La_2O_3$-i, respectively. For comparison, $Ir(4.8)/Al_2O_3$-i catalyst was prepared by replacing La_2O_3 with γ-Al_2O_3 (Zeolitechem Co., Ltd.) and controlling the Ir loading as 4.8 wt% with the above-mentioned procedure.

As far as ultrasonic-assisted impregnation method was concerned, $IrCl_3{\cdot}nH_2O$ and citric acid were dissolved into distilled water to obtain a brown solution. Under ultrasonic condition at 300 W (Ultrasonic Processors VCX 750, Sonics & Materials, Inc.), La_2O_3 and H_2O_2 were introduced in sequence, and the latter was added dropwise. The molecular ratio of $IrCl_3{\cdot}nH_2O$:citric acid:H_2O_2:La_2O_3 was 1:2:1:6. Then the system was sonicated for another 15 min until a light blue suspension was obtained, indicating that Ir^{3+} was oxidized to Ir^{4+} [34]. The resulting catalyst was dried at 120 °C overnight, and then calcined at 500 °C in argon for 2 h. The catalyst was denoted as $Ir(9)/La_2O_3$-s.

2.2. Catalyst characterizations

Since La_2O_3 tends to form hydrated $La_2(CO_3)_3$ when exposed to damp air [29], the reduced or used samples were cooled down to room temperature under N_2 atmosphere and sealed prior to characterization. Specific-surface-areas of supported Ir catalysts were measured by N_2 adsorption at liquid N_2 temperature (ASAP 2010, Micromeritics). Before the measurement of surface area, the samples were degassed at 300 °C in vacuum overnight. X-ray diffraction experiments (D/max-IIIA, Rigaku) were carried out from 5° to 90° with a step-size of 0.02° and a counting time of 2 s. The FTIR spectra were obtained using a Nicolet 380 FT-IR spectrometer equipped with a DTGS–CsI detector and a CsI beamsplitter. The samples were scanned 32 times with a resolution of 4 cm^{-1}. TEM and HRTEM images were obtained in JEM-2010/2010F (JEOL) microscopes equipped with INCA Energy Dispersive Spectrometer (Oxford Instruments) operating at 200 kV. Specimens for TEM and HRTEM were prepared by ultrasonically suspending the sample in acetone and depositing a drop of the suspension onto a grid. X-ray photoelectron spectroscopy (XPS) was performed with a Kratos Axis ultra (DLD) equipped with Al Kα X-ray source. The binding energies (±0.2 eV) were referenced to the C_{1s} peak at 284.6 eV due to adventitious carbon.

H_2 chemisorption experiments were carried out in an Auto Chem II chemisorption Analyzer. 0.2 g catalyst sample was firstly reduced in a flow of H_2/Ar (10 vol% of H_2) at 500 °C for 40 min at a ramping rate of 10 °C/min. After purging with Ar for 10 min, the sample was cooled down to 50 °C in argon. The adsorption of hydrogen was carried out by pulsing H_2/Ar (10 vol% of H_2) until saturation. Hydrogen consumption was detected by a thermal conductivity detector (TCD). The particle size can be calculated by: $d = 6M/(6.02 \times 10^{23}{\cdot}\rho\sigma D)$, where d is the diameter of Ir particle in nanometers (nm), M is the relative molecular weight of Ir (192.22), ρ is the density of Ir (22.5 g/cm^3), σ is the occupied area of a Ir atom (~0.01 nm^2), and D is the dispersion defined as the fraction of surface atom.

2.3. Catalytic reaction

Catalytic tests were performed in a quartz fixed-bed reactor with a preheater. In each experiment, 0.1–0.2 g catalysts were sandwiched with quartz wool and packed in the reactor. A thermocouple was inserted into the center of the catalytic bed to monitor the reaction temperature. Before the reaction, the catalyst was activated with hydrogen of 50 ml/min at 500 °C for 40 min. Then, a mixture of ethanol and water with 1:3 molar ratio was fed into the preheater by a syringe pump at a flow rate of 0.1 ml/min, and vaporized at 140 °C. For OSRE reaction, air at room temperature was introduced and mixed with the gaseous reactant at the inlet of the reactor. The molar ratio of ethanol to oxygen was 1:0.83. The gas hourly space velocity (GHSV) was 5×10^4 h^{-1}. As the performance of $Ir(9)/La_2O_3$-i was compared with that of $Ir(9)La_2O_3$-s, a GHSV of 1.9×10^5 h^{-1} was also used. The reaction temperature was 450–700 °C. For comparison, SRE reaction was also carried out over $Ir(9)/La_2O_3$-i under the same conditions as those of OSRE at GHSV = 5×10^4 h^{-1} except for the introduction of air at 650 °C for 3 h. The corresponding GHSV was 3.6×10^4 h^{-1}.

The reformate was analyzed by an Agilent 6820 GC equipped with Haysep (for the analysis of ethanol, acetaldehyde, water, acetone, CO_2, and C_2H_4) and 13× molecular sieve (for H_2, N_2, CO, and CH_4) packed columns. N_2 was used as the inert standard to calculate the mass balances. The carbon balances of GC analysis were within 100 ± 8%. The ethanol conversion and product selectivities were calculated by:

$$X_{\text{Ethanol}} = \frac{F_{\text{Ethanol, in}} - F_{\text{Ethanol, out}}}{F_{\text{Ethanol,in}}},$$

$$S_{\text{H}_2} = \frac{F_{\text{H}_2\text{ out}}}{(6-2\delta) \times F_{\text{Ethanol, in}} \times X_{\text{Ethanol}}},$$

$$S_{\text{i}} = \frac{m \times F_{\text{i, out}}}{2 \times F_{\text{Ethanol, in}} \times X_{\text{Ethanol}}},$$

where F is the normal flow rate, m is the number of carbon atoms in a product molecule, and δ is the stoichiometric number of O_2 in OSRE reaction:

$$C_2H_5OH + \delta O_2 + (3-2\delta)H_2O \rightarrow (6-2\delta)H_2 + 2CO_2.$$

3. Results and discussion

3.1. Evolution of catalyst support over Ir/La_2O_3-i catalyst

Fig. 1 presents the XRD spectra of $Ir(9)/La_2O_3$-i catalyst at various conditions. The fresh $Ir(9)/La_2O_3$-i sample shows diffraction peaks from hydrated $La_2(CO_3)_3$. The absence of Ir^0 or IrO_2 peaks indicates that complex or amorphous structures may be formed.

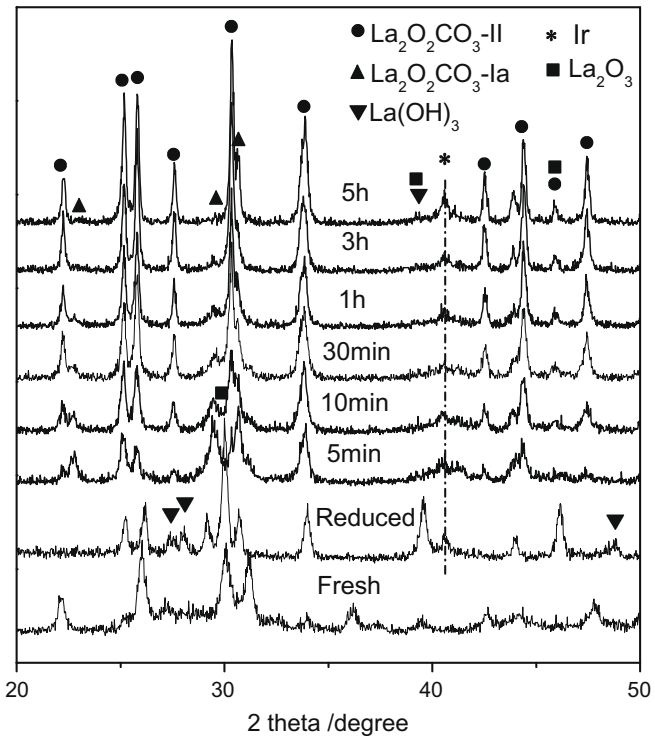

Fig. 1. XRD spectra of fresh, reduced, and used Ir(9)/La_2O_3-i catalysts for 5, 10, and 30 min, 1, 3, and 5 h on stream. OSRE reaction conditions: EtOH:O_2:H_2O = 1:0.83:3, GHSV = 5×10^4 h^{-1}, 650 °C.

After reduction with hydrogen, the (1 0 0) plane peak of cubic Ir appeared. Meanwhile, diffraction peaks from three La-containing species appeared, i.e. La_2O_3, $La_2O_2CO_3$-II, and $La(OH)_3$, among which La_2O_3 dominated. The peaks of La_2O_3 disappeared after 5 min at 650 °C, while the peaks of Ia and II-type $La_2O_2CO_3$ became stronger, indicating that La_2O_3 was converted into $La_2O_2CO_3$ rapidly under OSRE conditions. With reaction time elapsed, the peaks of $La_2O_2CO_3$-Ia gradually diminished, and those of $La_2O_2CO_3$-II enhanced, indicating that $La_2O_2CO_3$-Ia was transformed into $La_2O_2CO_3$-II. The formation and evolution of dioxymonocarbonate $La_2O_2CO_3$ during the OSRE reaction was also verified by FTIR spectroscopy (see Fig. S1 in Supplementary material). In this paper, although the support was mainly $La_2O_2CO_3$ during the reaction, we denoted the catalyst as Ir/La_2O_3 for convenience.

The transformation of La_2O_3 to $La_2O_2CO_3$ has been observed in several reactions [18,22,35]. Carbon-containing species, such as coke, CO_2 and CH_4, can contribute to the formation of $La_2O_2CO_3$. Among the I, Ia, and II-type $La_2O_2CO_3$ polymorphs, the $La_2O_2CO_3$-II is the most stable one and the other two can transform into II type above 400 °C [29]. Thus, the transformation of Ia to II-type $La_2O_2CO_3$ polymorph was probably due to the high temperature employed here. The formation of $La_2O_2CO_3$ has been suggested positive to eliminate the coke around metal particles, thereby preventing the deactivation of Ni catalyst from coking in SRE [18]. Our results show that La_2O_3 as a carbon reservoir is so effective that La_2O_3 is completely converted to $La_2O_2CO_3$ within a short reaction time. As shown in Fig. 2, coke can be clearly observed in TEM image of used Ir(4.8)/Al_2O_3-i, whereas not any carbon deposit can be found in used Ir(9)/La_2O_3-i.

3.2. Formation of Ir-doped $La_2O_2CO_3$ over Ir/La_2O_3-i catalyst

Besides the excellent coking resistance of Ir/La_2O_3-i, the TEM observation also indicates that the nanoparticles on the used Ir(9)/La_2O_3-i sample are uniformly dispersed. The average size of

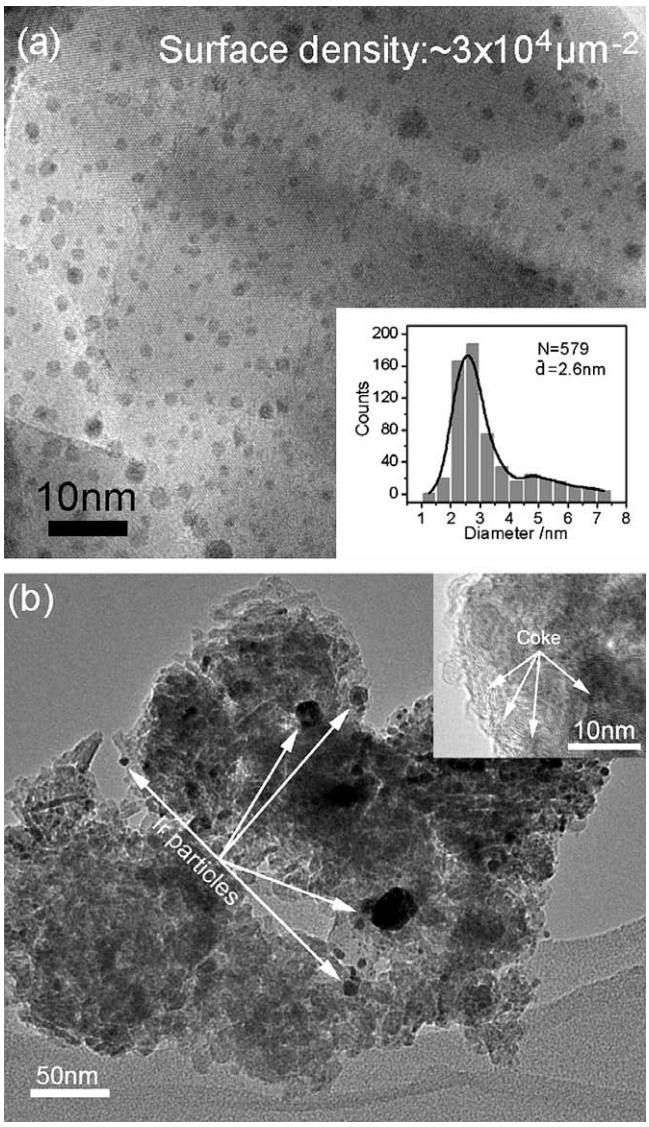

Fig. 2. TEM images of the used (a) Ir(9)/La_2O_3-i and (b) Ir(4.8)/Al_2O_3-i catalysts. The histogram of particle diameter of Ir(9)/La_2O_3-i is shown in the inset of (a). OSRE reaction conditions: EtOH:O_2:H_2O = 1:0.83:3, GHSV = 5×10^4 h^{-1}, 650 °C, time on stream of 3 h.

these nanoparticles is 2.6 nm, as shown in Fig. 2a. Although Ir(4.8)/Al_2O_3-i has lower metal loading, much larger particles, with size of 5–50 nm, were formed (Fig. 2b). Taking into account the low specific-surface-area of La_2O_3 compared with that of Al_2O_3 (Table 1), the ability of Ir(9)/La_2O_3-i to form such uniformly dispersed nanodomains is quite interesting and astonishing.

HRTEM analysis was performed to determine the composition and structure of these nanodomains, as shown in Fig. 3a and c. Most of the fringes from support can be attributed to the (1 0 1), (1 0 2), and (1 0 3) planes of $La_2O_2CO_3$-II. Interestingly, the HRTEM observation of the nanoparticles supported on $La_2O_2CO_3$-II shows that there exist two types of nanoparticles with different crystalline characteristics. The fringes in the domains highlighted by solid lines are accordant with the (1 0 0) plane of metallic iridium. However, the fringe intervals of the particles highlighted by dashed lines showed that they are well accordant with (1 0 3), (1 1 0), (1 0 7), and (1 1 4) planes of $La_2O_2CO_3$-II. The corresponding Fourier Transform (FFT) images also present clear diffraction patterns of metallic Ir and $La_2O_2CO_3$-II. The above-mentioned results indicate that a portion of the nanoparticles possess crystalline charac-

Table 1
Specific-surface-areas of the oxide supports and the fresh Ir catalysts.

Catalyst	Al_2O_3	Ir(4.8)/Al_2O_3-i	La_2O_3	Ir(4.8)/La_2O_3-i	Ir(9)/La_2O_3-i	Ir(9)/La_2O_3-s
S_{BET} ($m^2\ g^{-1}$)	168.5	126.6	11.9	5.7	1.6	3.6

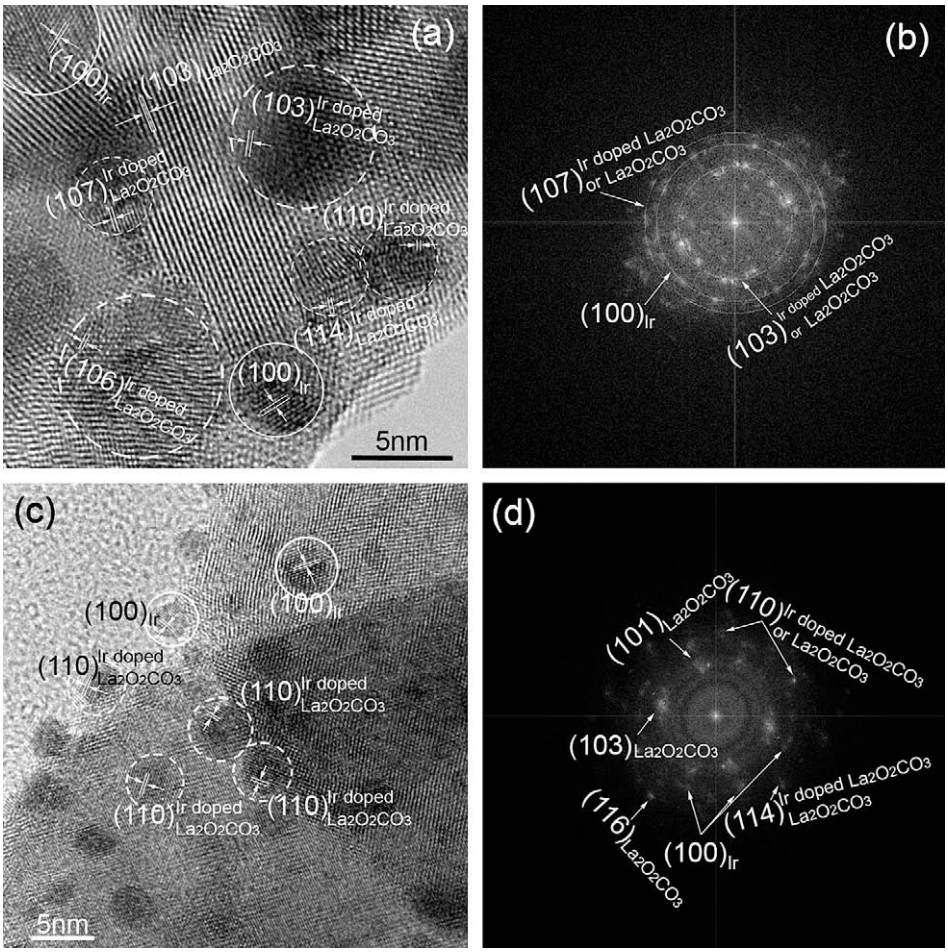

Fig. 3. HRTEM images (a and c) and corresponding Fast Fourier Transform results (b and d) of the used Ir(9)/La_2O_3-i. OSRE reaction conditions: EtOH:O_2:H_2O = 1:0.83:3, GHSV = $5 \times 10^4\ h^{-1}$, 650 °C, time on stream of 3 h.

teristics similar to those of $La_2O_2CO_3$-II support. The micro-area EDS analysis indicated that these domains contained La, C, O, and Ir, implying the formation of a complex composed of Ir and lanthanum species.

Due to the limitation of spatial resolution of EDS and the influence of support on the FFT images, XPS was employed to obtain the catalyst surface information. Ir_{4f} spectra of the fresh, reduced, and used (for 30 min and 3 h OSRE reaction) Ir(9)/La_2O_3-i catalysts are shown in Fig. 4a, b, d, and e. The $Ir_{4f7/2}$ peak of fresh Ir(9)/La_2O_3-i centers at 63.4 eV, which is much higher than that of IrO_2 (about 61.8 eV [36,37]). Combined with the XRD pattern (Fig. 1), it can be rationally deduced that the strong interaction between Ir and La species resulted in the formation of Ir–La–O complex during the preparation procedure. After activation by H_2, the Ir–La–O complex in fresh catalyst would be reduced to form metallic Ir^0, as evidenced by the shift of $Ir_{4f7/2}$ to 60.7 eV [37,38]. However, the Ir_{4f} spectra of used Ir(9)/La_2O_3-i show that a part of the metallic Ir would be converted into compounds with higher valence $Ir^{\delta+}$ after OSRE reaction at 650 °C for 30 min. The deconvolution of the Ir_{4f} spectrum in Fig. 4d shows that the area ratio of Ir^0 to $Ir^{\delta+}$ is ~0.3, as shown in Table 2, indicating that most of the Ir^0 was converted into $Ir^{\delta+}$ within 30 min. Combining with the HRTEM observation, it is rational to assign the complex particles depicted in Fig. 3 as the $Ir^{\delta+}$ species, demonstrating the coexistence of Ir and Ir–La–C–O complex particles during OSRE reaction.

The above-mentioned results also imply that the chemical nature of surface Ir was influenced by the reaction atmosphere. As shown in Fig. 4c, after shutting off the air supply, i.e. SRE reaction, only Ir^0 can be detected in used Ir(9)/La_2O_3 by XPS. This indicates that the Ir–La–C–O complex tends to be formed in oxidative conditions, whereas the reductive conditions favor the formation of Ir^0. It should also be noted that the Ir–La–C–O complex particles might be unstable during the reaction, because the area ratio of Ir^0 to $Ir^{\delta+}$ increased to ~0.8 after 3 h, indicating that part of the complex would decompose to release Ir^0. However, the complex existed even after the stable status was achieved (3 h in Fig. 4 and 100 h reaction in Table 2), suggesting the dynamic equilibrium between the formation and decomposition of the Ir-containing complex.

The above-mentioned results demonstrated that the active sites in Ir/La_2O_3-i possessed quite complicated chemical nature. It has been reported that $La_2O_2CO_3$-II/La_2O_3 can be doped by Li [33], Pt [19], Tb, Nd, and Y [39–41]. Attfield et al. proposed that the pres-

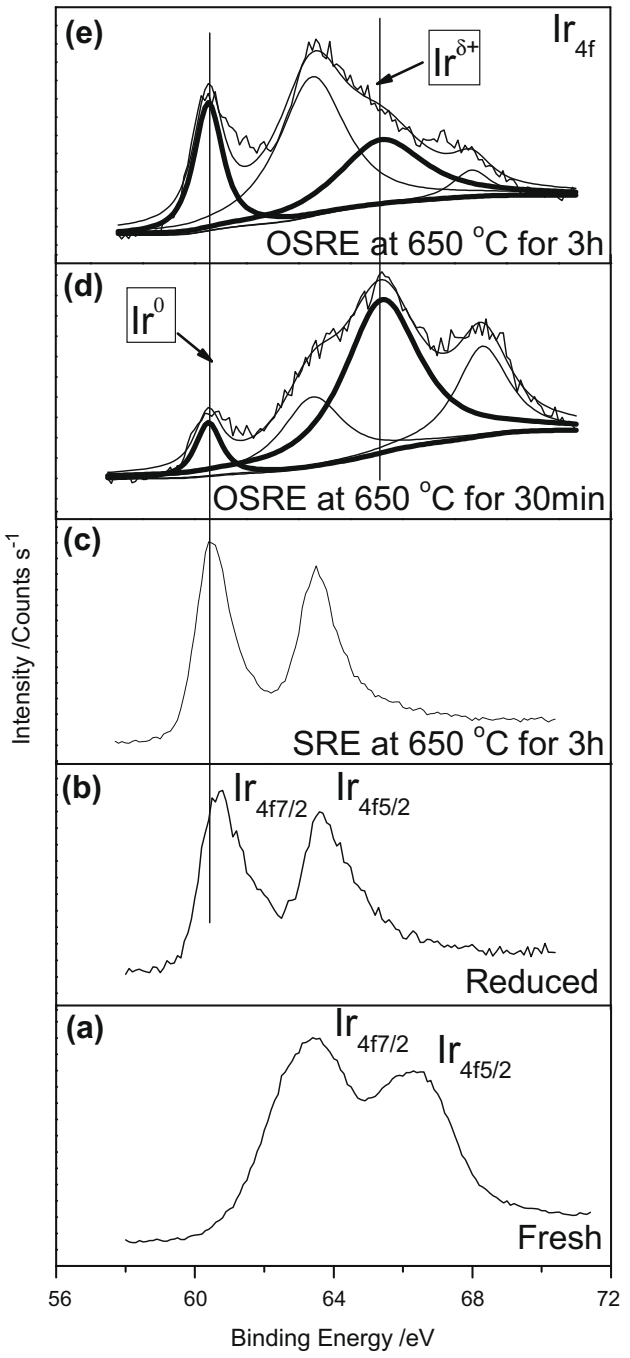

Fig. 4. Ir_{4f} core–shell spectra of (a) fresh, (b) reduced and used Ir(9)/La_2O_3-i catalysts for (c) SRE for 3 h, OSRE for (d) 30 min, and (e) 3 h. The spin-orbit splitting between $4f_{7/2}$ and $4f_{5/2}$ lines was constrained to 2.9 eV for deconvolution [36]. SRE reaction conditions: EtOH:H_2O = 1:3, GHSV = 3.6×10^4 h^{-1}, 650 °C. OSRE reaction conditions: EtOH:O_2:H_2O = 1:0.83:3, GHSV = 5×10^4 h^{-1}, 650 °C.

ence of ionic Li can induce vacancies of $(CO)^{2+}$ units, which may be inserted by Li to form Li-doped $La_2O_2CO_3$-II, while keeping its hexagonal crystal lattice [33]. Because the radius of Ir^{3+} ion (68 pm) is close to that of Li^{+1} ion (76 pm) [42], it can be expected that Ir-doped $La_2O_2CO_3$-II can be formed with the analogous mechanism. During the formation of $La_2O_2CO_3$-II, Ir^0 dispersed on the catalyst inserted into the lattice, which resulted in the $Ir^{\delta+}$ species being detected in XPS. When the incorporation of Ir did not destroy the framework of $La_2O_2CO_3$-II crystallites, structure and interplane distances similar to those of $La_2O_2CO_3$-II would be observed, as shown in Fig. 3. Delivering the active metallic sites via solid solution or perovskite has been widely applied in the high temperature reactions, such as CH_4 reforming reaction [22,27,43] and nanomaterial synthesis [44], where the size control of active sites is important. Our findings present an *in situ* formation mechanism of Ir-doped $La_2O_2CO_3$ through SIMS between Ir and La species, which will effectively improve the dispersion of metals. As will be demonstrated in the text that follows , this results in higher performance for OSRE reaction.

3.3. In situ dispersion of Ir during the OSRE reaction

We have shown that highly dispersed Ir-containing domains were formed through Ir-doped $La_2O_2CO_3$ during the OSRE reaction. XRD was used to investigate the change of Ir particle size during the reaction for understanding the process. In the current stage, we cannot rule out that the Ir-doped $La_2O_2CO_3$ may act as an active site of OSRE directly. But it is rational to study the evolution of active sites by representing them with Ir, due to the prevailing content of Ir^0 in long-term stable catalyst.

As shown in Fig. 5a, the apparent crystallite sizes of Ir and $La_2O_2CO_3$-II were determined by Scherrer's equation using the (1 0 0) reflection for iridium and the (1 1 0) one for $La_2O_2CO_3$-II. The particle size at the beginning of the reaction was represented by that of the reduced sample. Under flowing N_2 at 650 °C for 3 h, namely without any reaction, the Ir size slightly increased from 18 to 22 nm, which is indicative of conventional thermal sintering. However, the size of Ir crystallite decreased significantly from 18 to 4.5 nm during the first half hour of OSRE reaction, and then increased gradually within the next 4.5 h. After 5 h OSRE, the size of the Ir crystallite was 12.6 nm, which was smaller than that of the reduced sample. This course was also revealed by H_2 chemisorption. Compared with XRD, the chemisorption measurement gave larger values. This may be caused by the reduction treatment at 500 °C before the H_2 chemisorption of used catalysts, which would induce aggregation among Ir domains. However, a similar tendency, i.e. the significant decrease of Ir particle size during the first 30 min, is well consistent with the XRD results.

The $La_2O_2CO_3$-II grain grew quickly during the first 1 h, ascertaining that the formation of Ir-doped $La_2O_2CO_3$ was induced during the transformation from La_2O_3 to $La_2O_2CO_3$-II, and then slowly in the next 4 h. In this process, the Ir size might be influenced by (1) the formation of Ir-doped $La_2O_2CO_3$ consuming Ir^0 and resulting

Table 2
Surface element concentrations and Ir/La, $Ir^0/Ir^{\delta+}$ atom ratios of the selected catalysts by XPS analysis.

	Reaction time	Ir (wt%)	La (wt%)	C (wt%)	O (wt%)	Ir/La	$Ir^0/Ir^{\delta+}$
Ir(9)La_2O_3-i	OSRE, 30 min	15.4	40.2	22.7	21.7	0.3	0.3
	OSRE, 3 h	16.1	40.3	22.8	20.8	0.3	0.8
	SRE, 3 h	14.9	49.6	6.3	29.2	0.2	–
Ir(9)La_2O_3-s	OSRE, 10 min	25.3	33.5	22.9	18.3	0.5	0.7
	OSRE, 3 h	23.4	26.7	30.9	19.0	0.6	0.5
	OSRE, 100 h	26.0	31.7	23.2	19.2	0.6	1.3

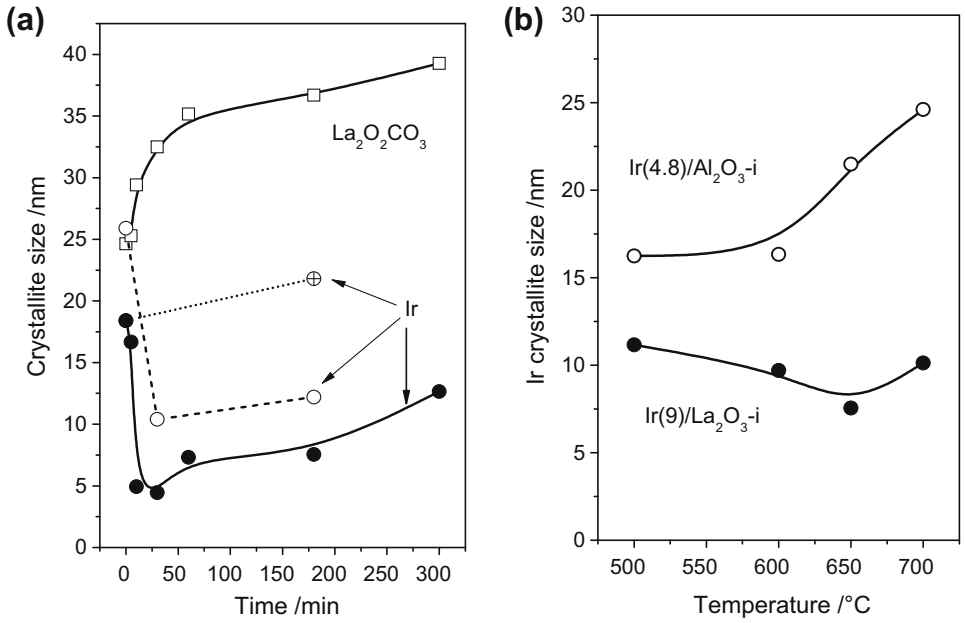

Fig. 5. $La_2O_2CO_3$-II and Ir crystallite sizes of Ir(9)/La_2O_3-i and Ir(4.8)/Al_2O_3-i as functions of (a) time on stream and (b) temperature. OSRE reaction conditions: EtOH:O_2:H_2O = 1:0.83:3, GHSV = 5×10^4 h^{-1}, 650 °C. The time on stream in (b) was fixed at 3 h. Symbols for Ir size in (a): ● in OSRE by XRD, ○ in OSRE by H_2 chemisorption, ⊕ reduced Ir(9)/La_2O_3-i exposed to N_2 atmosphere at 650 °C.

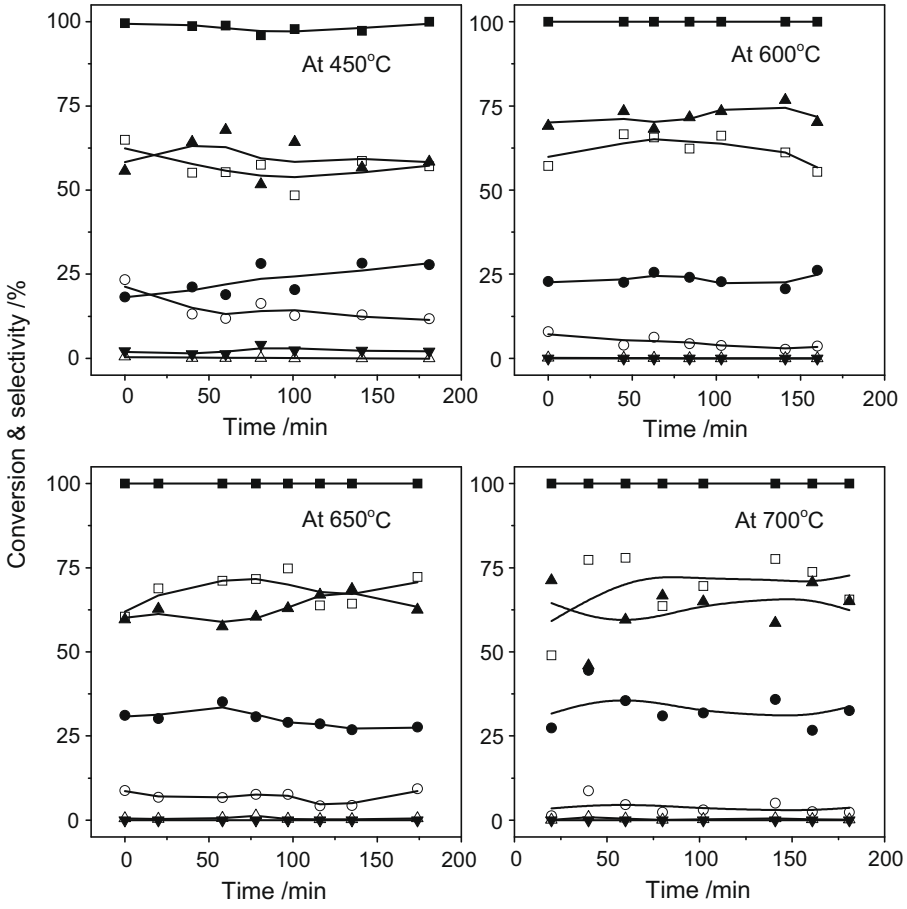

Fig. 6. The OSRE performances of Ir(4.8)/La_2O_3-i catalyst at 450, 600, 650, and 700 °C. OSRE reaction conditions: EtOH:O_2:H_2O = 1:0.83:3, GHSV = 5×10^4 h^{-1}. Conversion (■); selectivities to H_2 (□), CO (●), CH_4 (○), CO_2 (▲), C_2H_4 (△) and C_2H_4O (▼).

in the reduction of Ir particles, and (2) thermal sintering of Ir. In the first hour, the high rate of the former resulted in the decrease of Ir size. Since the formation and decomposition of $La_2O_2CO_3$-II are reversible [18], Ir^0 would be released again through the decomposition of $La_2O_2CO_3$-II. Therefore, once the transformation of La_2O_3 to $La_2O_2CO_3$-II was completed, the relatively high sintering rate

led to the increase of Ir size. However, during the decomposition of the Ir-doped $La_2O_2CO_3$, the $La_2O_3/La_2O_2CO_3$ may separate the Ir particles by neighboring them, which can effectively inhibit the sintering of Ir particles. Finally, a dynamic equilibrium between the above-mentioned two factors will be accomplished. Thus, a smaller Ir particle size was achieved after 5 h reaction. This effect afforded a novel mechanism to disperse active sites *in situ* and spontaneously, which played a vital role in the formation and stabilization of Ir sites.

The *in situ* dispersion effect upon Ir/La_2O_3-i can be further demonstrated by the dependence of Ir crystallite size on reaction temperature, as shown in Fig. 5b. Differing from the conventional sintering process of metals, the Ir crystallite size decreased with reaction temperature in the range from 500 to 650 °C. From 650 to 700 °C, an increase of Ir size was observed. However, the size at 700 °C is also smaller than that at 500 °C. This unique temperature dependence of $Ir(9)/La_2O_3$-i led to a quite narrow variation of Ir size from 7 to 11 nm within a wide temperature range, indicating an excellent sintering resistance. Compared with the minor sintering of $Ir(9)/La_2O_3$-i, that of $Ir(4.8)/Al_2O_3$-i above 600 °C resulted in a serious increase of Ir crystallite size from 16 to 25 nm. This unique behavior of $Ir(9)/La_2O_3$-i can be explained by the dependence of pyrolysis rate of Ir-doped $La_2O_2CO_3$-II on temperature. Since the high temperature accelerated the kinetics of the reversible decomposition-formation process, the *in situ* dispersion effect decreased Ir size in the range of 500–650 °C. The increase at 700 °C was due to the higher sintering rate at higher temperatures. Since the minimum of Ir crystallite size was achieved at 650 °C, it can be expected that good OSRE performances will be accomplished under this condition.

3.4. OSRE performances of Ir/La_2O_3-i

Figs. 6 and 7 show the OSRE performances of $Ir(4.8)/La_2O_3$-i and $Ir(4.8)/Al_2O_3$-i at 450–700 °C (see also Fig. S2 in Supplementary material for the performances of $Ir(9)/La_2O_3$-i). OSRE on $Ir(4.8)/La_2O_3$-i produced H_2, CO_2, CO, and CH_4 as main gaseous products. Quite a few C_2H_4O were detected at 450 °C, indicating that the dehydrogenation reaction took place. The selectivity toward H_2 increased progressively with temperature, because the steam reforming reaction of methane was enhanced, meanwhile the CO selectivity increased due to the suppressed water-gas shift (WGS) reaction at high temperatures. In the temperature range between 450 and 700 °C, the conversion and selectivities were stable over $Ir(4.8)La_2O_3$-i within 3 h.

Compared with the hydrogen selectivity of $Ir(4.8)/La_2O_3$-i, that of $Ir(4.8)/Al_2O_3$-i was lower; meanwhile obvious deactivation of catalyst was observed at 450 °C, which may be attributed to the deposition of coke on the surface of the catalyst (see Fig. 2b). The stable activities and selectivities were achieved at 650 °C within 3 h. However, continuous elevation of temperature to 700 °C resulted in a serious decrease of H_2 selectivity with time on stream. Combining with the significant increase of CO selectivity, it can be proposed that the sites responsible for WGS undergo transformation, due to the coking over acidic Al_2O_3 support or sintering of Ir, as demonstrated in the former sections.

As predicted by the *in situ* dispersion mechanism over Ir/La_2O_3-i, the above-made comparison demonstrates the superior activity, selectivity, and stability of Ir catalyst on $La_2O_2CO_3$-II to that on conventional Al_2O_3 support. The advantages of Ir/La_2O_3-i resulted from: (1) the highly dispersed catalytic domains affording better

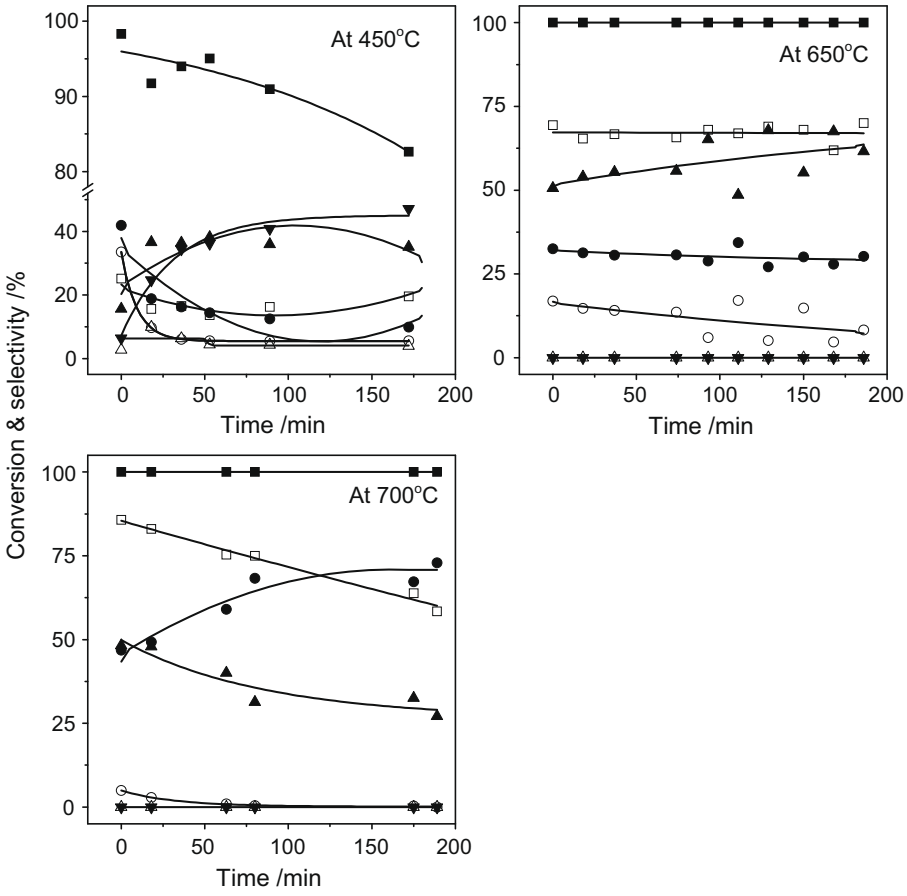

Fig. 7. The OSRE performances of $Ir(4.8)/Al_2O_3$-i catalyst at 450, 650, and 700 °C. OSRE reaction conditions: $EtOH:O_2:H_2O = 1:0.83:3$, $GHSV = 5 \times 10^4\ h^{-1}$. Conversion (■); selectivities to H_2 (□), CO (●), CH_4 (○), CO_2 (▲), C_2H_4 (△) and C_2H_4O (▼).

activity, (2) the formation of $La_2O_2CO_3$-II eliminating the coke, and (3) the *in situ* dispersion effect preventing Ir sintering. It can be expected that the above-mentioned understanding will provide useful principles for the design and optimization of OSRE catalysts, which is verified by the later studies.

3.5. Enhanced OSRE performances of Ir/La_2O_3-s catalyst

For precious metal catalysts, obtaining high metal dispersion is important for high performances. However, this is usually limited by sintering at elevated temperatures, especially on supports with low specific-surface-area. The above-mentioned results from Ir/La_2O_3-i suggest a new way to improve the dispersion at high temperatures through the *in situ* dispersion effect, which can maintain the initial metal dispersion via the Ir-doped $La_2O_2CO_3$ during OSRE. Thus, one can expect that Ir/La_2O_3 catalyst with higher initial metal dispersion will be more active and also stable. Ultrasound has been successfully applied in nanomaterial synthesis [45]. Since the acoustic cavitation generates localized hotspots with transient temperatures of ~5000 K and pressures of ~1800 atm [46,47], the ultrasound can prevent aggregation of the nanometer-sized clusters and isolate the nanoparticles [48]. In this work, ultrasound has been employed to assist the dispersion of Ir during the impregnation.

The low and high magnification TEM images of the used Ir(9)/La_2O_3-s catalyst are shown in Fig. 8. Compared to the Ir(9)/La_2O_3-i catalyst without ultrasonication, the denser and well-dispersed particles with a mean size of about 3.8 nm were observed, which resulted in an increase of surface density from $\sim 3 \times 10^4$ to $\sim 4 \times 10^4\ \mu m^{-2}$ (defined as the particle number per square micron). The HRTEM analysis and XPS spectra also demonstrated that these particles were a mixture of Ir and Ir-doped $La_2O_2CO_3$ (not shown). The increase of surface Ir concentration was well supported by the quantitative XPS analysis, as shown in Table 2. The surface Ir concentration significantly increased from around 15% to 25% as the ultrasonic-assisted impregnation method was applied. These results demonstrated the success of increasing the Ir dispersion over catalyst surface via the ultrasonic-assisted impregnation method. The higher dispersion of Ir due to ultrasonication could be explained by homogeneous nucleation. Ir could be oxidated and deposited onto lanthanum oxide support surface quickly before it is agglomerated in the solution. Lanthanum oxide species could react with Ir oxide to form Ir–La–O or Ir–La–C–O species during the preparation procedure, which prevent Ir from sintering during calcination. Thus, ultrasonication could result in a better dispersion of Ir.

A similar *in situ* dispersion phenomenon was revealed on the Ir(9)/La_2O_3-s catalyst by XPS and XRD. As shown in Table 2, the $Ir^0/Ir^{\delta+}$ ratio varied from 0.5 at 3 h to 1.3 at 100 h of time on stream, indicating the evolution of Ir-doped $La_2O_2CO_3$ through its reversible formation and decomposition. However, the long exposure (100 h on stream) in OSRE reaction did not decrease the surface concentration of Ir, indicating that the dispersion of active site was not deteriorated through sintering. As shown in Fig. 9, the Ir crystallite size calculated by XRD in Ir(9)/La_2O_3-s was 4.5 nm at a OSRE time of 10 min, which is much smaller than that in Ir(9)/La_2O_3-i, demonstrating the effect of ultrasonication on the formation of highly dispersed catalyst. The size increased to 6.6 nm within the first 3 h on stream. We speculated that it was probably due to the aggregation caused by the high surface density of active sites. However, after the completion of the transformation of La_2O_3 to $La_2O_2CO_3$-II (evidenced by the small change of $La_2O_2CO_3$-II

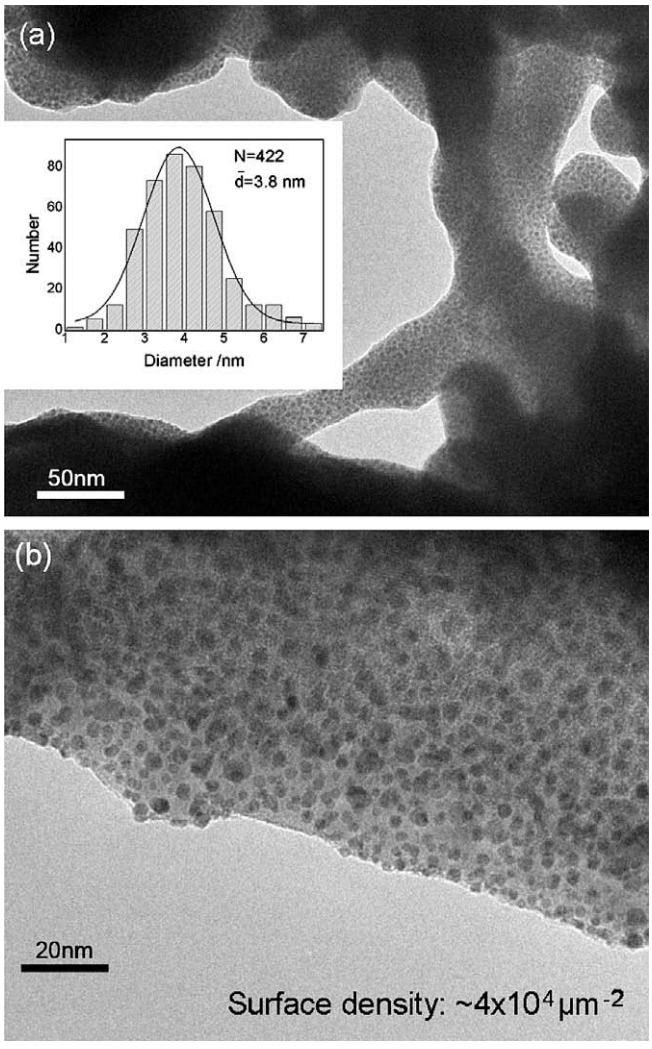

Fig. 8. (a) Low and (b) high magnification TEM images of the used Ir(9)/La_2O_3-s catalyst. The inset in (a) shows the histogram of diameter of surface particles. OSRE reaction conditions: EtOH:O_2:H_2O = 1:0.83:3, GHSV = $5 \times 10^4\ h^{-1}$, 650 °C, 30 min on stream.

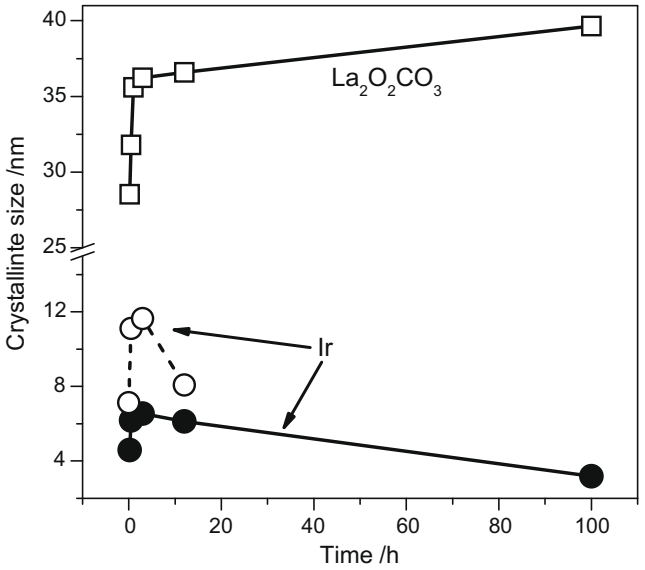

Fig. 9. $La_2O_2CO_3$-II and Ir crystallite sizes of Ir(9)/La_2O_3-s as functions of time on stream. OSRE reaction conditions: EtOH:O_2:H_2O = 1:0.83:3, GHSV = $5 \times 10^4\ h^{-1}$, 650 °C. Symbols for Ir size: ● by XRD, ○ by H_2 chemisorption.

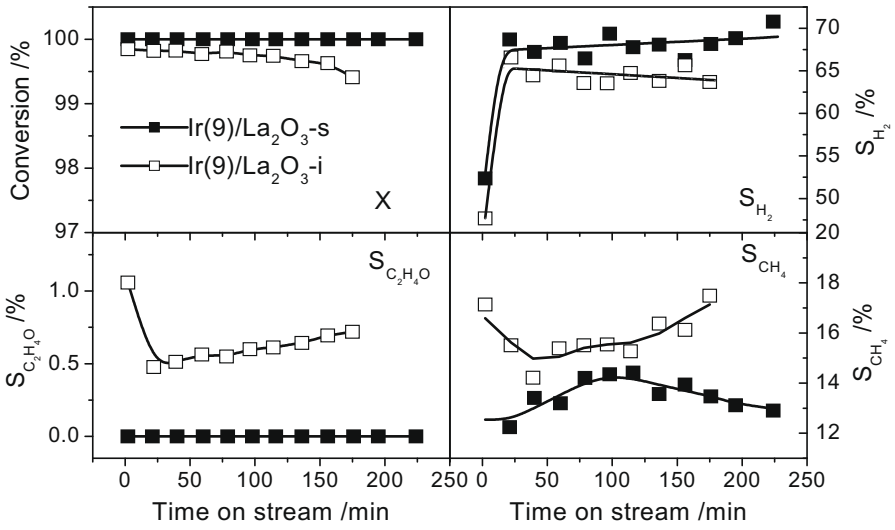

Fig. 10. The comparison of OSRE performances of Ir(9)/Lal$_2$O$_3$-i and Ir(9)/Lal$_2$O$_3$-s catalysts. OSRE reaction conditions: EtOH:O$_2$:H$_2$O = 1:0.83:3, GHSV = 1.9×10^5 h^{-1}, 650 °C.

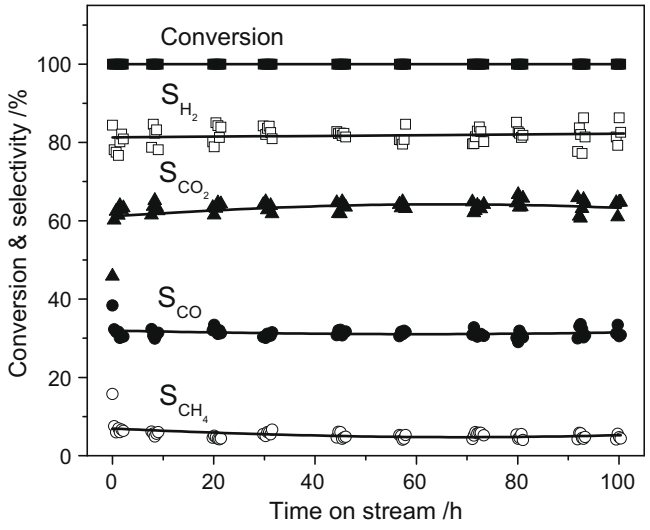

Fig. 11. Stability of Ir(9)/La$_2$O$_3$-s catalyst. OSRE reaction conditions: EtOH:O$_2$:H$_2$O = 1:0.83:3, GHSV = 5×10^4 h^{-1}, 650 °C.

crystallite size), the Ir crystallite size gradually decreased to 3.2 nm at 100 h on stream due to the *in situ* dispersion effect. A similar tendency was also revealed by the H_2 chemisorption method, except for the larger values caused by the H_2 reduction treatment, as discussed in Section 3.3. This is in accordance with the prediction by the insight into the interaction between Ir and La species, and affords a method to control the sintering of metal particles and to give a stable catalyst for the high temperature reaction.

Fig. 10 compares the OSRE performances of Ir(9)/La$_2$O$_3$-i and Ir(9)/La$_2$O$_3$-s catalysts under a high GHSV of 1.9×10^5 h^{-1}. On Ir(9)/La$_2$O$_3$-s sample, a complete conversion of ethanol with a selectivity of ~69% to hydrogen was obtained. No acetaldehyde was produced over Ir(9)/La$_2$O$_3$-s. As predicted by the above-mentioned account, the lower conversion and H_2 selectivity were observed on Ir(9)/La$_2$O$_3$-i. Deactivation was also observed for Ir(9)/La$_2$O$_3$-i under such a harsh GHSV condition. It was noted that 0.5 vol% ethylene was detected after 1.5 h on Ir(9)/La$_2$O$_3$-i, meanwhile the selectivities to acetaldehyde and methane increased with time. This suggested that the deactivation may be caused by the insufficient reformation of intermediates, which resulted in more coke deposition that can not be gasified by La$_2$O$_2$CO$_3$. Even under this high GHSV, the gradual decrease of Ir sizes with time was also observed (see Fig. S3 in Supplementary material). The OSRE reaction stability of the Ir(9)/La$_2$O$_3$-s catalyst is shown in Fig. 11. The Ir(9)/La$_2$O$_3$-s catalyst was stable with time on stream of 100 h without any drop of conversion and H_2 selectivity. The average H_2 selectivity during 100 h was 81.8%, which is higher than that over Ir(9)/La$_2$O$_3$-i as more CH_4 was reformed by steam. Correspondingly, the H_2 yield per molecular ethanol was about 3.5 mol/mol$_{EtOH}$, which is close to the thermodynamics limitation [49,50] under this feedstock composition. These results validated the insight into the *in situ* dispersion effect of Ir over La$_2$O$_2$CO$_3$-II and provided a valuable approach to design an efficient OSRE catalyst.

4. Conclusions

Physicochemical characterizations showed that La$_2$O$_3$ was transformed into La$_2$O$_2$CO$_3$-II during the OSRE reaction. Ir reacted with La$_2$O$_2$CO$_3$-II strongly, leading to the formation of Ir-doped La$_2$O$_2$CO$_3$-II, which was well dispersed on the La$_2$O$_2$CO$_3$-II support surface. The dynamic formation and decomposition of Ir-doped La$_2$O$_2$CO$_3$-II *in situ* delivered and dispersed Ir metal particles at elevated temperatures. This process prevented the Ir/La$_2$O$_3$ catalyst from sintering and from aggregation of Ir nanoparticles, and therefore offered a superior activity and stability to the Al$_2$O$_3$-supported Ir catalyst.

Based on the insight into the *in situ* dispersion mechanism of Ir over La$_2$O$_2$CO$_3$-II, a supersonic-assisted impregnation method was used to improve the surface iridium concentration and reduce the initial Ir domain size. Since the *in situ* dispersion effect effectively inhibited the sintering, the Ir crystallite size was maintained at 3.2 nm after 100 h OSRE at 650 °C. This significantly enhanced the activity and stability of Ir/La$_2$O$_3$ catalysts for the OSRE reaction. The finding provides a novel and effective method to fabricate high performance metal catalysts for OSRE reaction at high temperatures.

Acknowledgments

This work was supported by the National High Technology Research and Development Program of China (863 Program, No. 2009AA05Z102) and the National Natural Science Foundation of

China (No. 50675070). The authors are grateful to Dr. Qiang Zhan (Tsinghua University) and Dr. Xiaobo Fu (The Hong Kong University of Science and Technology) for TEM measurements.

Appendix A. Supplementary material

Supplementary data associated with this article can be found, in the online version, at doi:10.1016/j.jcat.2009.11.010.

References

[1] F. Frusteri, S. Freni, J. Power Sources 173 (2007) 200.
[2] P.R. de la Piscina, N. Homs, Chem. Soc. Rev. 37 (2008) 2459.
[3] R.M. Navarro, M.A. Pena, J.L.G. Fierro, Chem. Rev. 107 (2007) 3952.
[4] E.C. Wanat, K. Venkataraman, L.D. Schmidt, Appl. Catal. A: Gen. 276 (2004) 155.
[5] A. Haryanto, S. Fernando, N. Murali, S. Adhikari, Energy Fuels 19 (2005) 2098.
[6] E.B. Pereira, N. Homs, S. Marti, J.L.G. Fierro, P.R. de la Piscina, J. Catal. 257 (2008) 206.
[7] S. Cavallaro, V. Chiodo, S. Freni, N. Mondello, F. Frusteri, Appl. Catal. A: Gen. 249 (2003) 119.
[8] F. Frusteri, S. Freni, V. Chiodo, S. Donato, G. Bonura, S. Cavallaro, Int. J. Hydrogen Energy 31 (2006) 2193.
[9] W. Cai, B. Zhang, Y. Li, Y. Xu, W. Shen, Catal. Commun. 8 (2007) 1588.
[10] J. Llorca, N. Homs, J. Sales, J.L.G. Fierro, P.R. de la Piscina, J. Catal. 222 (2004) 470.
[11] A.J. Vizcaino, P. Arena, G. Baronetti, A. Carrero, J.A. Calles, M.A. Laborde, N. Amadeo, Int. J. Hydrogen Energy 33 (2008) 3489.
[12] F. Can, A. Le Valant, N. Bion, F. Epron, D. Duprez, J. Phys. Chem. C 112 (2008) 14145.
[13] E.C. Wanat, B. Suman, L.D. Schmidt, J. Catal. 235 (2005) 18.
[14] J.R. Salge, G.A. Deluga, L.D. Schmidt, J. Catal. 235 (2005) 69.
[15] G.A. Deluga, J.R. Salge, L.D. Schmidt, X.E. Verykios, Science 303 (2004) 993.
[16] J. Kugai, V. Subramani, C.S. Song, M.H. Engelhard, Y.H. Chin, J. Catal. 238 (2006) 430.
[17] B.C. Zhang, W.J. Cai, Y. Li, Y.D. Xu, W.J. Shen, Int. J. Hydrogen Energy 33 (2008) 4377.
[18] A.N. Fatsikostas, D.I. Kondarides, X.E. Verykios, Catal. Today 75 (2002) 145.
[19] J.C.S. Araujo, D. Zanchet, R. Rinaldi, U. Schuchardt, C.E. Hori, J.L.G. Fierro, J.M.C. Bueno, Appl. Catal. B 84 (2008) 552.
[20] M.C. Sanchez-Sanchez, R.M. Navarro, J.L.G. Fierro, Int. J. Hydrogen Energy 32 (2007) 1462.
[21] M.C. Sanchez-Sanchez, R.M. Navarro, J.L.G. Fierro, Catal. Today 129 (2007) 336.
[22] G.S. Gallego, F. Mondragon, J.M. Tatibouet, J. Barrault, C. Batiot-Dupeyrat, Catal. Today 133 (2008) 200.
[23] C. Batiot-Dupeyrat, G. Valderrama, A. Meneses, F. Martinez, J. Barrault, J.M. Tatibouet, Appl. Catal. A: Gen. 248 (2003) 143.
[24] G.S. Gallego, F. Mondragon, J. Barrault, J.M. Tatibouet, C. Batiot-Dupeyrat, Appl. Catal. A: Gen. 311 (2006) 164.
[25] G.S. Gallego, C. Batiot-Dupeyrat, J. Barrault, F. Mondragon, Ind. Eng. Chem. Res. 47 (2008) 9272.
[26] S.M. de Lima, I.O. da Cruz, G. Jacobs, B.H. Davis, L.V. Mattos, F.B. Noronha, J. Catal. 257 (2008) 356.
[27] M.E. Rivas, J.L.G. Fierro, M.R. Goldwasser, E. Pietri, M.J. Perez-Zurita, A. Griboval-Constant, G. Leclercq, Appl. Catal. A: Gen. 344 (2008) 10.
[28] K. Nakagawa, N. Ikenaga, Y.H. Teng, T. Kobayashi, T. Suzuki, Appl. Catal. A: Gen. 180 (1999) 183.
[29] R.P. Turcotte, J. Sawyer, L. Eyring, Inorg. Chem. 8 (1969) 238.
[30] A.N. Shirsat, M. Ali, K.N.G. Kaimal, S.R. Bharadwaj, D. Das, Thermochim. Acta 399 (2003) 167.
[31] V.A. Tsipouriari, X.E. Verykios, J. Catal. 187 (1999) 85.
[32] R.M. Navarro, M.C. Alvarez-Galvan, M.C. Sanchez-Sanchez, F. Rosa, J.L.G. Fierro, Appl. Catal. B 55 (2005) 229.
[33] J.P. Attfield, G. Férey, J. Solid State Chem. 82 (1989) 132.
[34] P.G. Hoertz, Y.I. Kim, W.J. Youngblood, T.E. Mallouk, J. Phys. Chem. B 111 (2007) 6845.
[35] T. Le Van, M. Che, J.M. Tatibouët, M. Kermarec, J. Catal. 142 (1993) 18.
[36] G.K. Wertheim, H.J. Guggenheim, Phys. Rev. B 22 (1980) 4680.
[37] K. Nakagawa, N. Ikenaga, T. Suzuki, T. Kobayashi, M. Haruta, Appl. Catal. A: Gen. 169 (1998) 281.
[38] T. Marzialetti, M. Oportus, D. Ruiz, J.L.G. Fierro, P. Reyes, Catal. Today 133 (2008) 711.
[39] T. Masui, K. Koyabu, S. Tamura, N. Imanaka, J. Mater. Sci. 40 (2005) 4121.
[40] A. Olafsen, A.K. Larsson, H. Fjellvag, B.C. Hauback, J. Solid State Chem. 158 (2001) 14.
[41] N. Imanaka, T. Masui, Y. Mayama, K. Koyabu, J. Solid State Chem. 178 (2005) 3601.
[42] J.A. Dean, Lange's Handbook of Chemistry, 15th ed., McGraw-Hill, New York, 1999.
[43] H. Provendier, C. Petit, C. Estournes, S. Libs, A. Kiennemann, Appl. Catal. A: Gen. 180 (1999) 163.
[44] P. Coquay, E. De Grave, A. Peigney, R.E. Vandenberghe, C. Laurent, J. Phys. Chem. B 106 (2002) 13186.
[45] A. Gedanken, Ultrason. Sonochem. 11 (2004) 47.
[46] K.S. Suslick, Science 247 (1990) 1439.
[47] E.B. Flint, K.S. Suslick, Science 253 (1991) 1397.
[48] K.S. Suslick, M. Fang, T. Hyeon, J. Am. Chem. Soc. 118 (1996) 11960.
[49] S. Liu, K. Zhang, L.N. Fang, Y.D. Li, Energy Fuels 22 (2008) 1365.
[50] G. Rabenstein, V. Hacker, J. Power Sources 185 (2008) 1293.